A New EMI Modeling Method for Mixed-Mode Noise Analysis in Three-Phase Inverter System

WU ZHOU, XUEJUN PEI [iD], **(Senior Member, IEEE), YANGXIAO XIANG** [iD], **AND YONG KANG**

State Key Laboratory of Advanced Electromagnetic Engineering and Technology, School of Electrical and Electronic Engineering, Huazhong University of Science and Technology, Wuhan 430074 China

Corresponding author: Xuejun Pei (ppei215@mail.hust.edu.cn)

ABSTRACT A novel frequency-domain EMC modeling technique is proposed to predict the conducted electromagnetic interference (EMI) in a three-phase inverter system. On the basis of the frequency-domain model, a three-terminal behavior model for analyzing mixed-model (MM) noise is derived. Different from the traditional model, the CM and DM noise sources are independent of each other, thus help to understand the MM phenomenon directly. It is shown that three stray capacitors in the IGBT module determine the amplitude of the MM noise, and the influence of the load current on the traditional CM and DM noise sources can be used for the MM noise observation. The simulation and experimental results are illustrated to verify the prediction technique and the MM noise analysis is confirmed.

INDEX TERMS Conducted electromagnetic interference (EMI), EMI modeling, mixed-mode (MM) noise, three-phase inverter.

I. INTRODUCTION

Pulse width modulated (PWM) converters are being widely used in both industrial and military applications for their high efficiency and reliability. However, they are also known to cause a number of major electromagnetic interference (EMI) problems due to the fast switching actions. In parallel soft-switched drive systems, the conducted EMI noise travels along the input and output power lines and causes interference with other electronic systems. In addition, the high value of dv/dt may cause high frequency ground leakage current, motor shaft voltage and the ensuing bearing current leading to bearing failure. As for radiated emission, the electromagnetic interference signals can be transmitted from the EMI noise source to the susceptible unit and bring problems such as communication errors, degraded equipment performance and malfunction or non-operation [1]–[3]. To avoid interference between different systems, the EMI noise emissions generated from such converters needed to be limited and complied with certain EMC regulations [4]. Usually, these standards are published by organizations such as European Norm (EN), International Electrotechnical Commission (IEC), International Special Committee on

Radio Interference (CISPR) and Australian and New Zealand (AS/NZS) [5], [6].

More details about the standards can be found in [7]–[9]. Thus the EMI filters are inevitably part for the EMI noise attenuation. As we all know, EMI modeling is the basis for developing EMI mitigation solutions. High frequency modeling of power converters is needed to analyze EMI and also optimize the EMI filter design.

Earlier works on EMI modelling of power converters usually use lumped circuits to model high frequency behavior of the circuits [10]–[12]. This technique is called time-domain modelling and requires detailed information of all the internal and parasitic impedances in the circuits and the physics-based models of the semiconductor devices, which may not be available. Moreover, a small time-step must be taken in the time-domain simulation for its accuracy, thus making it very slow. In [11] and [12], the semiconductor devices are replaced by trapezoidal sources, but such simplifications will limit the accuracy of the models.

Frequency-domain modelling techniques have been developed in [13]–[20]. In [13]–[15], an elementary commutation cell, which is referred to the EMI source, is replaced by two sources shown in Fig. 1. The differential model (DM) emission seen from the dc side is modelled by a current source i_{dc}. The common model (CM) emission is modelled by a voltage

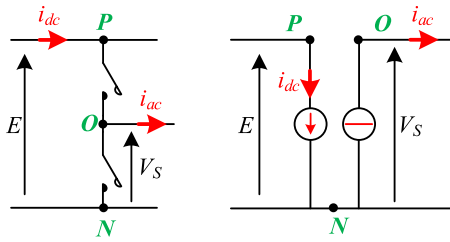The associate editor coordinating the review of this manuscript and approving it for publication was Atif Iqbal [iD].

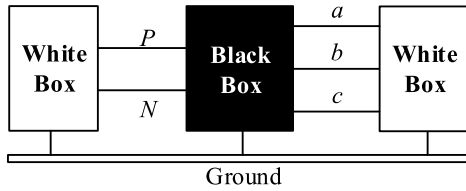**FIGURE 1.** EMI equivalent source model of a commutation cell.

FIGURE 2. Behavioral modeling equivalent circuit.

FIGURE 3. Modeling procedures of the inverter system.

source V_s. Thus the DM and CM noise equivalent circuits can be got respectively and separately. In [16], it is shown that such models have a limitation when mixed-mode noise becomes significant, especially in the case with converters that are asymmetric with respect to ground. In [17]–[20], the frequency-domain behavioral modelling techniques are developed. These techniques treat some parts of the system as a "black box" and use a generic noise, usually a Thevenin or Norton equivalent circuit to replace it, as shown in Fig. 2. Such models have a limitation when the "black box" is to be understood.

In real application, there exists an additional noise-coupling mode, called the mixed-mode (MM), which should be taken into consideration in the EMI modeling process. The non-intrinsic DM noise in a fly-back converter system is firstly identified as the MM noise by S. Qu and D. Chen in [21]. Further studies focus on the mitigation of the MM noise in the fly-back system can be found in [21]–[25]. There are also some papers discussing the MM noise in the three-phase inverter system. In [26], the MM noise on the AC side is analyzed while the MM noise on dc side is ignored. In [27], the EMI behavioral model of a three-phase power inverter system has been got to analyze the MM noise, but the model can only be got by experiment and is hard to be understood.

In this paper, a novel frequency-domain EMC modeling technique is proposed [28]. Based on the proposed model, CM and DM noise sources and propagations are analyzed respectively. Then a three-terminal behavior model for analyzing the MM noise is derived from the proposed model. It is found that three stray capacitors of the IGBT module dominate the MM noise. Moreover, the influence of the load current on CM and DM noise sources can be used for the MM noise observation.

This paper is organized as follows. A frequency-domain model of the three-phase inverter system is proposed
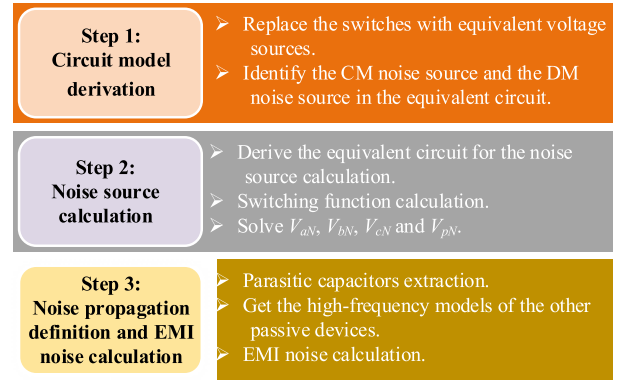
in Section II. Section III analyzes the MM noise in the three-phase inverter system based on the proposed model. In Section IV, simulation and experiment results are presented to validate the analysis. Finally, a conclusion is drawn in Section V.

II. FREQUENCY-DOMAIN MODELING PROCEDURE

The frequency-domain model of the inverter system can be got on the base of superposition theorem. The modeling procedures consist of three steps:

Step 1: Derive the circuit model of the inverter system.

Step 2: Calculate the EMI noise source in the inverter system.

Step 3: Identify the noise propagation and calculate the EMI noise of the total system.

More details can be found in Fig. 3.

A. CIRCUIT MODEL DERIVATION

Fig. 4 shows the detailed circuit model of the three-phase inverter system. In the circuit, the main parasitic parameters are taken into account. C_P and C_N represent the total common mode dc bus stray capacitors if the bus stray inductors between each bridge (L_{bus}) are neglected. C_O represents the total stray capacitor of the midpoint of each bridge. C_{Cg} represents the total common mode stray capacitor of the output filter with respect to the ground.

The principle of the modeling is to replace the switches with equivalent sources. According to the substitution theorem, if the IGBTs VTx and $\overline{VTx}$ ($x \in \{a, b, c\}$) are substituted by the voltage sources having the same voltage waveforms, the circuit behavior keeps the same. Thus, the six switch branches can be replaced by six voltage sources. Furthermore, if ignoring the bus inductors, the six voltage sources can be reduced to four ones further. Fig. 5 shows the resultant circuit, which is the circuit model for the conducted EMI prediction. Traditional studies treat the DM noise source as a current source and ignore the bus stray capacitors C_P and C_N, thus the mixed-mode noise is out of consideration [14]. On the other hand, the circuit model shows in Fig. 5 takes the bus stray capacitors into consideration and can be used for
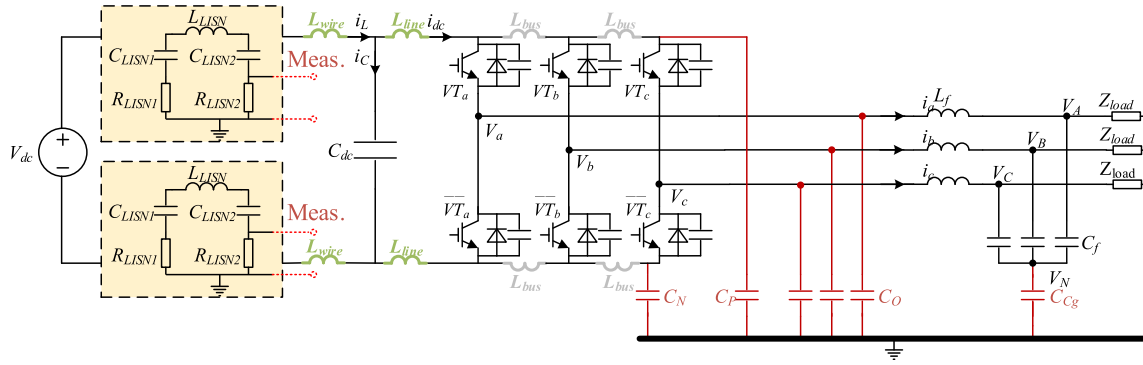
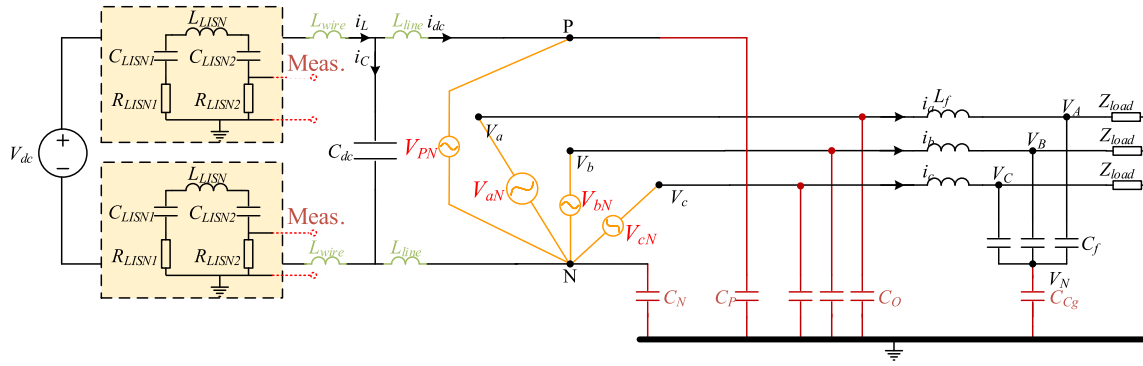**FIGURE 4.** Detailed circuit model of a three-phase inverter system.

FIGURE 5. EMC prediction circuit model of a three-phase inverter system.

mixed-mode noise analysis. In Fig. 5, V_{PN} represents the equivalent DM noise source V_{DM}. V_{aN}, V_{bN} and V_{cN} represent the three equivalent CM noise sources. Moreover, due to the symmetry of the three bridge branches, three CM noise sources can be replaced by the equivalent voltage V_{CM} shown in (1).

$$V_{CM} = (V_{aN} + V_{bN} + V_{cN})/3 \qquad (1)$$

B. NOISE SOURCE CALCULATION

In the three-phase inverter system shown in Fig. 4, the output voltage of each bridge varies from 0 V to V_{dc}. As a result, V_{CM} is the most dominating noise source. Noise source V_{PN} also contributes to the total noise source. The noise source in frequency-domain can be obtained from measurement or simulation. The measurement can just be taken after the prototype is setup. Thus, the simulation method is selected and the procedures are presented in detail in this paper.

In order to calculate the noise source, the equivalent circuit is simplified as Fig. 6. In Fig. 6, V_{dc} represents the voltage through the dc-link capacitor, L_{line} represents the inductance of the cable between the dc-link capacitor and the phase-A bridge, and Z_l represents the total impedance of the output filter and the load. Based on the theory of Kirchoff's voltage law (KVL) and Kirchoff's current law (KCL), the noise
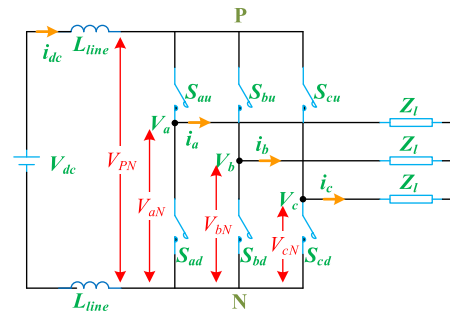

FIGURE 6. Simplify circuit for noise source calculation.

source can be solved by the following circuit equations

$$\begin{cases} V_{aN}(t) = V_{PN}(t) \times S_{au}(t) + 0 \times S_{ad}(t) = V_{PN}(t) \times S_{au}(t) \\ V_{bN}(t) = V_{PN}(t) \times S_{bu}(t) + 0 \times S_{bd}(t) = V_{PN}(t) \times S_{bu}(t) \\ V_{cN}(t) = V_{PN}(t) \times S_{cu}(t) + 0 \times S_{cd}(t) = V_{PN}(t) \times S_{cu}(t) \\ i_{dc}(t) = i_a(t) \times S_{au}(t) + i_b(t) \times S_{bu}(t) + i_c(t) \times S_{cu}(t) \end{cases}$$

$$(2)$$

$$\begin{cases} V_{aN}(s) - (V_{aN}(s) + V_{bN}(s) + V_{cN}(s))/3 = i_a(s) \times Z_l(s) \\ V_{bN}(s) - (V_{aN}(s) + V_{bN}(s) + V_{cN}(s))/3 = i_b(s) \times Z_l(s) \\ V_{cN}(s) - (V_{aN}(s) + V_{bN}(s) + V_{cN}(s))/3 = i_c(s) \times Z_l(s) \\ V_{dc}(s) - V_{PN}(s) = 2sL_{line} \times i_{dc}(s) \end{cases}$$
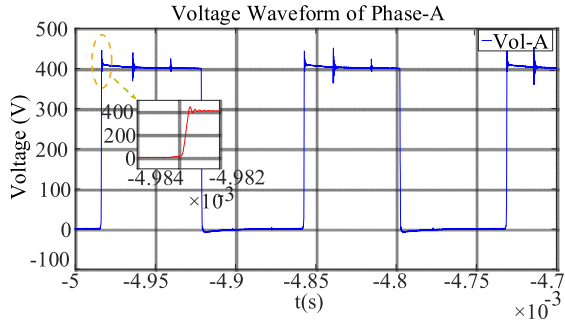
$$(3)$$

FIGURE 7. Experiment result of the output voltage waveform.

$$i_{dc}(s) = \frac{V_{dc}(s) - V_{PN}(s)}{2sL_{line}} \quad (4)$$

From (2) and (3) V_{PN}, V_{aN}, V_{bN} and V_{cN} can be solved both in time-domain and frequency-domain if the three switching functions S_{au}, S_{bu} and S_{cu} are known. Thus, the noise source can be got. It should be noted that V_{dc} keeps a constant voltage level for the existence of the dc-link decoupling capacitor, thus the DM current i_{dc} can be simply got from V_{PN} as shown in (4).

Due to the electromagnetic couplings among the parasitic parameters of the IGBTs and the dc bus, there exists high frequency ringing on the output voltage waveform in a real voltage source inverter system. These high frequency ringing waveforms are caused by switching actions in both self-phase and other phases. To precisely predict multiple ringing frequencies, all the parasitic parameters in the inverter system must be considered. More details to explain the high frequency ringing waveforms can be found in [29]. To make the noise source calculation procedure fast but not inaccurate, only the main harmonics in the ringing waveforms are considered. Fig. 7 shows the measured waveform of V_{aN}.

To model this ringing and make the calculation accurate. The high frequency ringing function can be expressed as

$$S_{Add} = \sum_{x=1,2,\cdots} M_{Ringx} \times e^{-t/T_{Dampx}} \times \sin(2\pi f_{Ringx}t) \quad (5)$$

where M_{Ringx} is the magnitude of the ringing, T_{Dampx} is the damping period, and f_{Ringx} is the ringing frequency, $x \in \{1, 2, \ldots\}$. Then the switching functions can be expressed as

$$S_{yu} = S_y + S_{Add} \quad (6)$$

where S_y denotes the traditional switching function, $y \in \{a, b, c\}$. It should be noted that x means different frequencies of harmonic appear in one resonance. The magnitude and the frequencies of the harmonics can be got easily by the experiment result of the output voltage waveform shown in Fig. 7.

C. NOISE PROPAGATION DEFINITION AND EMI NOISE CALCULATION

The accuracy of the parasitic parameters is the key to successful EMI prediction through simulation. Thus, the capacitors
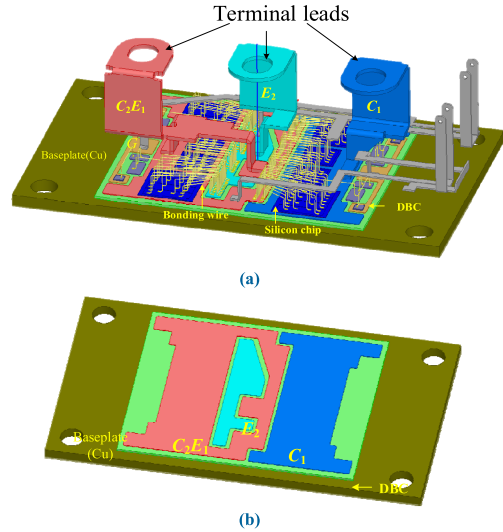

FIGURE 8. 3D structure model of 2MBI200S-120, (a) complete model (b) simplified model.

in Fig. 5 are especially important for the common mode noise generation. For the extraction of the parasitic capacitances, the simulation software used in this study is Simplorer 16.2 from ANSYS. The main parasitic capacitors are the stray capacitors of the IGBTs in the model.

The simulation model is made for IGBT component 2MBI200S-120, which is used in the experiment prototype. The 3D structure of the model is illustrated in Fig. 8. The collector of the IGBT chip and the cathode of the diode chip are mounted on the direct-bond-copper (DBC). Bonding wires are used to solder the IGBT and the diode chips to a conductor pad so that the emitter-to-anode connection can be made. The terminal leads are soldered on the required pad and introduced to the outside screw mounting holes and the gate and source connectors.

It should be noted that the 3D structure model represents the switches in one phase, which include both the upper switch and the lower switch. The right four silicon chips in deep blue represent the upper IGBT and diode. The left four silicon chips in deep blue represent the lower IGBT and diode. The junction capacitance of the upper IGBT and diode is the capacitance between the two surfaces of the right four silicon chips. The junction capacitance of the lower IGBT and diode can be got similarly.

Fig. 8 (b) shows a simplified 3D structure model of the IGBT module. The bonding wires and the terminal leads are ignored in this model. This simplification has no effect on the calculation of the capacitance. However, this simplified model cannot be used for parasitic capacitors extraction of the IGBT module for its neglect of junction capacitors. The simulation results of the capacitances are got from the 3D structure model shown in Fig. 8 (a). It should be noted that this simulation is independent from the EMI simulation of the total system, and the 3D structure model is just used for the extraction of the parasitic capacitors of the IGBT module.

TABLE 1. Comparison of the capacitances got from calculation, simulation and experiment.

	C_1	E_2	$C_2 E_1$
ε_0(F/m)		9.8	
ε		8.86×10^{-12}	
d(m)		6×10^{-4}	
A(m^2)	2.9591×10^{-3}	7.9836×10^{-4}	3.7412×10^{-3}
Cal.(pF)	428.23	115.53	541.41
Sim. (pF)	446.85	125.30	571.8
Exp.(pF)	464	124	610

The bonding wires in the 3D structure model are the key for the measurement of the parasitic capacitors of the IGBT module. The bonding wires are used to link the upper surfaces of the silicon chips to the terminal leads. When the bonding wires on the right side are removed, the link between the C_2E_1 terminal lead and the upper switches are disconnected. When the bonding wires on the left side are removed, the link between the E_2 terminal lead and the lower switches are disconnected. The measurement of the parasitic capacitors are down with all the bonding wires are removed. Thus the influence of junction capacitance can be eliminated. And the capacitance can be measured directly by the impedance analyzer.

The capacitances can be calculated using the commonly known formula:

$$c = \varepsilon_0 \varepsilon_r \frac{A}{d} \tag{7}$$

where ε_0 is the air dielectric constant, ε_r is the relative dielectric constant of the substrate material, A is the equivalent area, and d is the distance between the DBC bottom copper layer and the baseplate.

From (7) and the IGBT structure shown in Fig. 8(a), the stray capacitance of IGBT is dominated by the DBC. Thus, the capacitive model of the IGBTs can be simplified to Fig. 8(b). The simulation results of the capacitive model, the calculated capacitances, and the experiment results are compared in Table 1. Thus, the capacitances of C_P, C_N and C_O can be got. C_P is 1392 pF, C_N is 372 pF and C_O is 610 pF. It should be noted that C_P and C_N represent the total common mode dc bus stray capacitors. Thus, C_P is three times the value of the capacitance of C_1 and C_N is three times the value of the capacitance of E_2. While C_O is in same value as the capacitance of C_2E_1.

The high frequency models of the other passive devices can be simply got by the use of impedance analyzer. The measurement results are shown in Fig. 9. It should be noted that these results are got by eliminate the influence of the testing wires, which can be considered as ideal inductors. The results are used in the simulation later.

L_{wire} and C_{cg} can be simply got by the measurement of the impedance analyzer. L_{wire} is 12 μH, C_{Cg} is 20 pF. After the procedures above, all the parameters in Fig. 5 can be got.
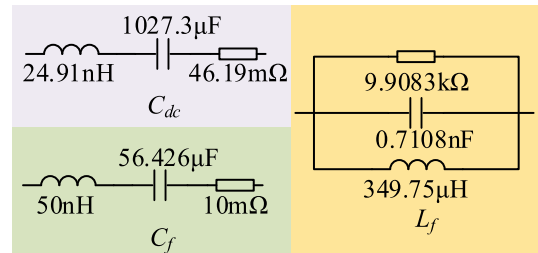

FIGURE 9. High frequency models of the passive devices.

The total EMI noise on LISNSs can be predicted through (8)

$$R(s) = \sum_{f=f_0, f_1, \cdots} Z(s) \times S(s), \quad s = j\omega f \tag{8}$$

where $R(s)$ is the total EMI noise to be predicted, $Z(s)$ is the voltage signal on LISNs produced by the unit magnitude noise source at each frequency, and $S(s)$ is the noise source in frequency-domain. It should be noted that the two noise sources V_{DM} and V_{CM} are included in $S(s)$. Moreover, $Z(s)$ and $S(s)$ are dominated by the propagation and the noise source respectively, thus can be studied in detail through the proposed model. The complete frequency-domain modeling procedure can be implemented by using Matlab and Saber cooperative simulation.

III. ANALYSIS OF THE MIXED-MODE EMI NOISE

According to the conventional theory, the DM noise is defined as the voltage difference between the two LISN resistors, and the CM noise is defined as the average voltage of the two LISN resistors. The CM and DM noises defined on LISNs are shown as

$$V_{DM}^N = V_u - V_d$$
$$V_{CM}^N = (V_u + V_d)/2 \tag{9}$$

where V_u and V_d are the voltage noise signals measured across the upward and downward LISNs respectively. The mixed-mode noise in this paper is defined as the noise caused by different type of noise source. For example, the CM noise caused by the DM noise source and the DM noise caused by the CM noise source are both mixed-mode noises.

A. BEHAVIORAL MODEL DERIVATION FOR THE MIXED-MODE NOISE ANALYSIS

From the analysis in Section II, the complete circuit model of the three-phase inverter system for the EMI modeling can be obtained from Fig. 5. Based on the superposition theorem and the symmetry of the three bridge branches, the equivalent circuit can be simplified to Fig. 10. In Fig. 10, all high frequency parasitic parameters, including IGBTs, inductors and capacitors, are taken into consideration. L_{wire} represents the total inductance of the wire when dc side EMI filter is out of consideration.

In this Section, a terminal circuit model derived from Fig. 10 is proposed and used for the MM noise analysis. There are three terminals, terminal positive (P), terminal negative (N) and ground (G), in the three-phase inverter system
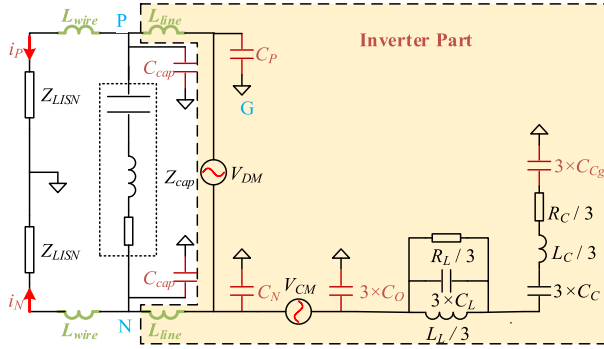
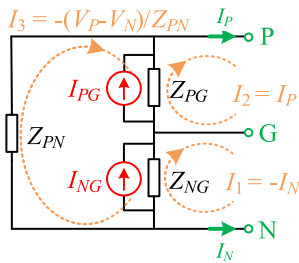**FIGURE 10.** Simplified equivalent circuit for analysis.

FIGURE 11. Simplest three-terminal circuit model.

when seeing from the dc side. Thus, a three-terminal model is needed to model the total inverter system from the dc side. As stated in [30], the simplest network that fully and uniquely defines a three-terminal system is composed of three impedances and two sources. It should be noted that the two sources are not fixed; furthermore, each source can be either voltage source or current source. Take two current sources for example, a simplest three-terminal circuit model can be got as shown in Fig. 11, in which the three impedances and the two current sources are independent of each other.

To model the entire inverter system, the first work is to model the inverter part shown in Fig. 10, then other parts of the system including the LISNs and the dc-link capacitor can be added to the three-terminal model directly. The inverter part can be equivalent to Fig. 12 through the circuit theorem, where the relations between the impedances and the sources of the two circuits can be expressed as

$$
\begin{cases}
Z_1 = Z_{L_{line}} \\
Z_2 = Z_{C_p} \\
Z_3 = Z_{C_N} || Z_{out} = Z_{C_N} || Z_{3 \times C_O} \\
V_1 = V_{DM} \\
V_2 = V_{CM} \dfrac{3C_O}{3C_O + C_N}
\end{cases}
\tag{10}
$$

Next work is to get the simplest three-terminal model of the inverter part and solve the five model parameters. The procedure of obtaining each component of the simplest three-terminal circuit model from those of the given one can be found in [29]. The details will be shown as follows.

The first step is to get the inner state equations. The original circuit shown in Fig. 12 has 5 branches and 5 nodes. The voltages and the currents of all the branches can specify a
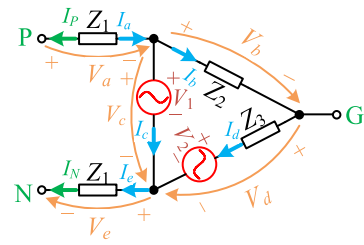

FIGURE 12. Equivalent circuit of the inverter part.

state of the circuit. Thus, there exist 10 state variables in the circuit. Among these 10 variables, there hold 4 equations by KCL and 1 equation by KVL. Furthermore, 5 more equations can be found in each branch by Ohm's law or given directly when the element is a source. To sum up, the 10 circuit state equations can be got as shown in (11).

$$
\begin{bmatrix}
0 & 1 & -1 & 1 & 0 & 0 & 0 & 0 & 0 & 0 \\
0 & 0 & 0 & 0 & 0 & 1 & 0 & 0 & 0 & 0 \\
0 & 0 & 0 & 0 & 0 & 1 & -1 & -1 & 0 & 0 \\
0 & 0 & 0 & 0 & 0 & 0 & 0 & 1 & 1 & -1 \\
0 & 0 & 0 & 0 & 0 & 0 & 0 & 0 & 0 & 1 \\
1 & 0 & 0 & 0 & 0 & -Z_1 & 0 & 0 & 0 & 0 \\
0 & 1 & 0 & 0 & 0 & 0 & -Z_2 & 0 & 0 & 0 \\
0 & 0 & 1 & 0 & 0 & 0 & 0 & 0 & 0 & 0 \\
0 & 0 & 0 & 1 & 0 & 0 & 0 & 0 & -Z_3 & 0 \\
0 & 0 & 0 & 0 & 1 & 0 & 0 & 0 & 0 & -Z_1
\end{bmatrix}
\begin{bmatrix}
V_a \\ V_b \\ V_c \\ V_d \\ V_e \\ I_a \\ I_b \\ I_c \\ I_d \\ I_e
\end{bmatrix}
$$

$$
=
\begin{bmatrix}
0 & 0 & 0 & 0 \\
0 & 0 & -1 & 0 \\
0 & 0 & 0 & 0 \\
0 & 0 & 0 & 0 \\
0 & 0 & 0 & 1 \\
0 & 0 & 0 & 0 \\
0 & 0 & 0 & 0 \\
0 & 0 & 0 & 0 \\
0 & 0 & 0 & 0 \\
0 & 0 & 0 & 0
\end{bmatrix}
\begin{bmatrix}
V_P \\ V_N \\ I_P \\ I_N
\end{bmatrix}
+
\begin{bmatrix}
0 \\ 0 \\ 0 \\ 0 \\ 0 \\ 0 \\ 0 \\ V_1 \\ V_2 \\ 0
\end{bmatrix}
\tag{11}
$$

The second step is to get the terminal state equations. The circuit shown in Fig. 12 has 3 terminals, P, N and G. Here take terminal G as the reference ground, then 2 terminal state equations can be got as shown in (12).

$$
\begin{bmatrix}
1 & 1 & 0 & 0 & 0 & 0 & 0 & 0 & 0 & 0 \\
0 & 0 & 0 & -1 & -1 & 0 & 0 & 0 & 0 & 0
\end{bmatrix}
\begin{bmatrix}
V_a \\ V_b \\ V_c \\ V_d \\ V_e \\ I_a \\ I_b \\ I_c \\ I_d \\ I_e
\end{bmatrix}
$$

$$
=
\begin{bmatrix}
1 & 0 & 0 & 0 \\
0 & 1 & 0 & 0
\end{bmatrix}
\begin{bmatrix}
V_P \\ V_N \\ I_P \\ I_N
\end{bmatrix}
+
\begin{bmatrix}
0 \\ 0
\end{bmatrix}
\tag{12}
$$

The last step is to get the terminal equations which include terminal variables V_P, V_N, I_P and I_N only. The 10 state variables can be solved by (11). Substituting the values of the 10 state variables into (12), we get the terminal equation as shown in (13). (13) can be further rewritten to (14), which shows the relations between the terminal variables.

$$
\begin{bmatrix}
-1 & 0 & -Z_1 - \dfrac{Z_2 Z_3}{Z_2 + Z_3} & -\dfrac{Z_2 Z_3}{Z_2 + Z_3} \\
0 & -1 & -\dfrac{Z_2 Z_3}{Z_2 + Z_3} & -Z_1 - \dfrac{Z_2 Z_3}{Z_2 + Z_3}
\end{bmatrix}
$$

$$
\times
\begin{bmatrix}
V_P \\ V_N \\ I_P \\ I_N
\end{bmatrix}
$$

$$
=
\begin{bmatrix} 0 \\ 0 \end{bmatrix}
-
\begin{bmatrix}
V_1 \dfrac{Z_2}{Z_2 + Z_3} - V_2 \dfrac{Z_2}{Z_2 + Z_3} \\
-V_1 \dfrac{Z_3}{Z_2 + Z_3} - V_2 \dfrac{Z_2}{Z_2 + Z_3}
\end{bmatrix}
\tag{13}
$$

$$
\begin{bmatrix} V_P \\ V_N \end{bmatrix}
+
\begin{bmatrix}
Z_1 + \dfrac{Z_2 Z_3}{Z_2 + Z_3} & \dfrac{Z_2 Z_3}{Z_2 + Z_3} \\
\dfrac{Z_2 Z_3}{Z_2 + Z_3} & Z_1 + \dfrac{Z_2 Z_3}{Z_2 + Z_3}
\end{bmatrix}
\begin{bmatrix} I_P \\ I_N \end{bmatrix}
$$

$$
=
\begin{bmatrix}
V_1 \dfrac{Z_2}{Z_2 + Z_3} - V_2 \dfrac{Z_2}{Z_2 + Z_3} \\
-V_1 \dfrac{Z_3}{Z_2 + Z_3} - V_2 \dfrac{Z_2}{Z_2 + Z_3}
\end{bmatrix}
\tag{14}
$$

As for the simplest three-terminal circuit model shown in Fig. 11, the relations between the terminal variables can be got by loop current analysis method. The result is shown in (15). By comparing (14) and (15), each component in Fig. 11 can be solved. The result is shown in (16). As stated above, Z_1 represents the total inductance of the wire between the dc-link capacitor and the phase-A bridge. Generally speaking, to make peak values of the voltages through the switches as small as possible, Z_1 is supposed to be small enough. In the inverter system stated in the paper, the inductance of Z_1 is smaller than 200 nH. Here take 200 nH as an extreme situation. From (16), Z_1 can be ignored only if Z_1 is far less than $2*(Z_2||Z_3)$. The spectrums of Z_1, $2*(Z_2||Z_3)$ and $Z_1 + 2*(Z_2||Z_3)$ are shown in Fig. 13. It shows that Z_1 can be ignored in the frequency range less than 5 MHz.

$$
\begin{bmatrix} V_P \\ V_N \end{bmatrix}
+
\begin{bmatrix}
\dfrac{Z_{PG}(Z_{NG} + Z_{PN})}{Z_{PG} + Z_{NG} + Z_{PN}} & \dfrac{Z_{PG} Z_{NG}}{Z_{PG} + Z_{NG} + Z_{PN}} \\
\dfrac{Z_{PG} Z_{NG}}{Z_{PG} + Z_{NG} + Z_{PN}} & \dfrac{Z_{NG}(Z_{PG} + Z_{PN})}{Z_{PG} + Z_{NG} + Z_{PN}}
\end{bmatrix}
$$

$$
\times
\begin{bmatrix} I_P \\ I_N \end{bmatrix}
$$

$$
=
\begin{bmatrix}
\dfrac{-Z_{PG}}{Z_{PG} + Z_{NG} + Z_{PN}} (I_{NG} Z_{NG} - I_{PG} Z_{NG} - I_{PG} Z_{PN}) \\
\dfrac{-Z_{NG}}{Z_{PG} + Z_{NG} + Z_{PN}} (I_{NG} Z_{PG} + I_{NG} Z_{PN} - I_{PG} Z_{PG})
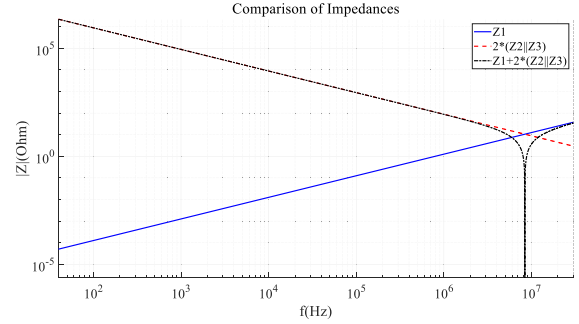\end{bmatrix}
\tag{15}
$$

FIGURE 13. Spectrum of Z_1, $2*(Z_2||Z_3)$ and $Z_1 + 2*(Z_2||Z_3)$.

$$
\begin{cases}
Z_{PG} = Z_{NG} = Z_1 + \dfrac{2 Z_2 Z_3}{Z_2 + Z_3} \approx 2(Z_2||Z_3) \\[2mm]
Z_{PN} = Z_1 \left(Z_1 \dfrac{Z_2 + Z_3}{Z_2 Z_3} + 2 \right) = Z_{PG} \dfrac{Z_1(Z_2 + Z_3)}{Z_2 Z_3} \approx 2Z_1 \\[2mm]
I_{PG} = \dfrac{1}{Z_{PG}} \left(\dfrac{Z_2}{Z_2 + Z_3}(V_1 - V_2) + \dfrac{Z_2 Z_3}{Z_1(Z_2 + Z_3)} V_1 \right) \\[2mm]
I_{NG} = \dfrac{1}{Z_{NG}} \left(\dfrac{V_1 Z_3 + V_2 Z_2}{Z_2 + Z_3} + \dfrac{Z_2 Z_3}{Z_1(Z_2 + Z_3)} V_1 \right)
\end{cases}
\tag{16}
$$

From the analysis above, the two current sources I_{PG} and I_{NG} have different values from each other, thus can be the sources of the MM noise. On the other hand, the two impedances between PG and NG are the same. If we make the two current sources I_{PG} and I_{NG} have the same value with the opposite directions, then the sources between PG and NG will contribute to common noise only. The sources for the CM and DM noise separation can be got by (17). By this equivalence, the CM and DM noises can be generated by CM and DM noise sources separately. Substituting (16) into (17), the CM current noise source and the DM current noise source can be got as shown in (18). Thus, the final three-terminal circuit model of the total inverter system which including LISNs and the dc-link capacitor is derived as shown in Fig. 13. It should be noted that Z_{Ccap} and Z_{Cdc} can be added to the three-terminal circuit model directly.

$$
\begin{aligned}
I_{SCM} &= (I_{NG} - I_{PG})/2 \\
I_{SDM} &= I_{PG} + I_{NG}
\end{aligned}
\tag{17}
$$

$$
\begin{aligned}
I_{SCM} &= (V_1 Z_3 - V_1 Z_2 + 2V_2 Z_2)/2 Z_{PG}(Z_2 + Z_3) \\
I_{SDM} &= V_1(Z_1 + 2Z_2||Z_3)/2 Z_1 Z_{PG}
\end{aligned}
\tag{18}
$$

B. MIXED-MODE NOISE ANALYSIS

Usually, each phase of the LISNs can be represented by 50 Ω impedance. The total inductance of the wire L_{wire} can be ignored for its series connection with LISNs. Therefore, from the three-terminal circuit model shown in Fig. 14, the CM and DM noises can be got as

$$
V_{DM}^N \approx \frac{V_{DM}}{Z_{PG}} \left(\frac{1}{2} + \frac{Z_2||Z_3}{Z_1} \right) (2Z_1||Z_{Cdc}||2(Z_{LISN}||Z_{PG}))
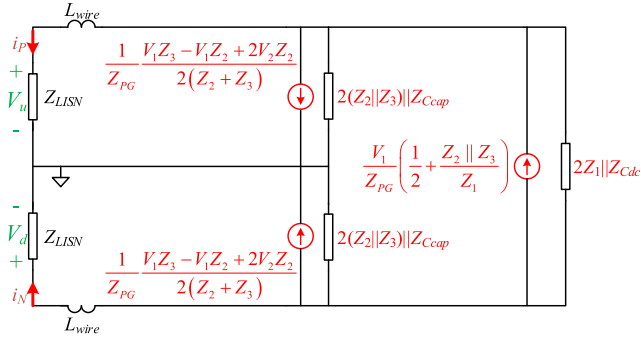$$

FIGURE 14. Final three-terminal circuit model for MM noise analysis.

$$V_{CM}^N \approx \frac{1}{Z_{PG}} \left(\frac{V_{DM}}{2} \frac{C_P - C_N - 3C_O}{C_P + C_N + 3C_O} \right.$$
$$\left. + V_{CM} \frac{3C_O}{C_P + C_N + 3C_O} \right)$$
$$\times (Z_{LISN}||Z_{PG}|| (2Z_1||Z_{Cdc} + Z_{LISN}||Z_{PG}))$$
$$\times \left(1 + \frac{Z_{LISN}||Z_{PG}}{Z_{LISN}||Z_{PG} + 2Z_1||Z_{Cdc}} \right) \qquad (19)$$

It should be noted that Z_{Ccap} is in parallel with Z_{LISN} thus can be ignored in the derivation process. As we can see in (19), the DM noise V_N DM is just dependent on the DM voltage noise source V_{DM}, which means that there is no MM noise. However, the CM noise V_N CM is dependent on both DM voltage noise source V_{DM} and CM voltage noise source V_{CM}. The CM noise which caused by the DM voltage noise source V_{DM} is the MM noise. In other words, the MM noise exists only in CM noise in the three-phase inverter system, if the circuit asymmetry of the propagation path is left out of consideration. Thus, the simulation and experiment results about the DM noise will not be shown later.

Another point is the influence of the MM noise on the total CM noise. From (19), it is clear that the three stray capacitors, C_P, C_N and C_O, dominate the weighting factors of the two voltage noise sources V_{DM} and V_{CM}. When the capacitances of the three capacitors are comparable, the weighting factors of both voltage noise sources are comparable to each other. If C_P and C_N are much larger than C_O, the weighting factor of V_{DM} will be much larger than that of V_{CM}. By this means, the MM noise can dominate the total CM noise.

In real situations, it is difficult to distinguish V_{DM} or V_{CM} from the total noise source. Thus it is difficult to measure the MM noise separately from the total CM noise. Fortunately, there exists a significant difference between the influence of the load current on V_{DM} and V_{CM}. This can be used for the MM noise observation later.

For the CM noise source V_{CM}, the load current does not affect the switching action and the resonance in the noise source, thus V_{CM} varies little with the load current. On the other hand, for the DM noise source V_{DM}, these exists a relation between the load current and the voltage of the dc bus V_{PN}, which is V_{DM}, as shown in (2) and (3). The load current i_a, i_b and i_c can influence the dc bus
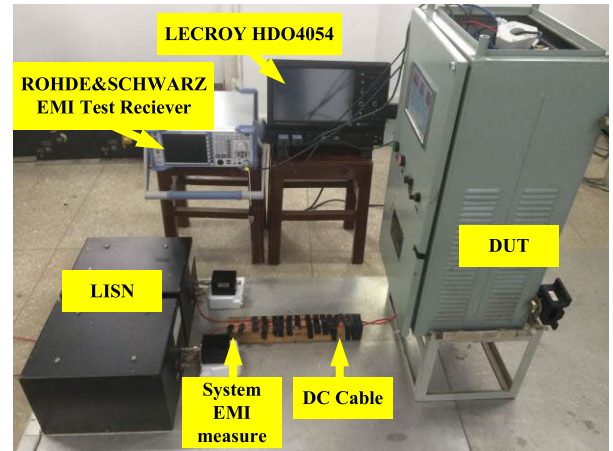

FIGURE 15. Test bench of the 12 kVA three-phase inverter system.

current i_{dc} through the switching functions, thus further affect the DM noise source V_{DM}. For the noise propagation, the frequency-domain characteristic waveform of the CM noise propagation will not change with the load situation for the symmetry of the three bridge branches, neither will that of the DM noise propagation change for the existence of the dc-link decoupling capacitor. To sum up, the load current can influence the total EMI noise on LISNs by affecting the DM noise source. This will be verified by simulation and experiment in next section.

IV. SIMULATION AND EXPERIMENT RESULTS

The simulation softwares used in this study are Saber and Matlab. Saber is a circuit simulation tool which here is used to simulate the EMI noise propagation mentioned above. Matlab is used as a calculation tool for EMI noise source generation as well as a data processing tool for EMI noise prediction.

It should be noted that both time-domain and frequency-domain images can be used for the analysis of EMI. But information about the frequency of the noise is just included in frequency-domain images, which is very important for EMI analysis. The changes about the amplitude of the EMI noise can also be directly presented in frequency-domain images. Moreover, EMC regulations provided by EMC standards are also in form of spectrum. Thus, spectrum is chosen as the only data processing tool in the simulation and experiment later.

A. TOTAL NOISE PREDICTION
Fig. 15 shows the 12 kVA three-phase inverter system test bench. The power converter is connected to the dc power supply through LISNs and dc cable. The power converter contains dc-link capacitor, bus-bar, three-phase H-bridge. Loads are connected with the power converter through output LC filter and ac cable. The inverter is designed to have the rated output voltages and currents of 380 V and 18 A at 400 V dc input. For simplicity, three-phase resistive load is used and connected to the inverter system in star formation. The output frequency is 50 Hz, and the switching frequency is 8 kHz.

TABLE 2. System parameters for simulation and experiment.

Parameter	Value	Parameter	Value
Switching Frequency	8 kHz	L_{wire}	12 μH
U_{dc}	400 V	C_P	1392 pF
C_{dc}	1030 μF	C_N	372 pF
L_{AC}	350 μH	C_O	610 pF
C_f	60 μF	C_{cg}	20 pF
R_{load}	15 Ω		
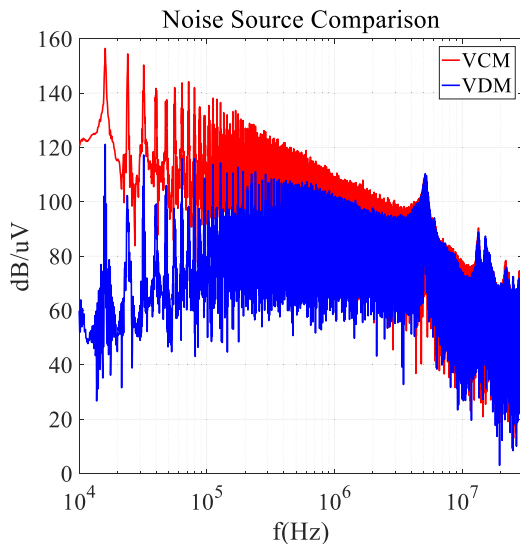
FIGURE 16. DM and CM noise sources got from simulation.

FIGURE 17. CM and DM noise sources for no load and full load, (a) CM noise source V_{CM} (b) DM noise source V_{DM}.

Some key system parameters are listed in Table 2. The circuit used in Saber is the same as that shown in Fig. 5 except that C_{cap} is taken into consideration. C_{cap} is 30 pF.

From the circuit equations given by (2), (3) and (4) in Section-II, V_{PN} is got by the difference between V_{dc} and the voltage through L_{line}. V_{dc} is the voltage through the dc-link capacitor. It can be considered as a constant in low frequencies. L_{line} represents he inductance of the cable between the dc-link capacitor and the phase-A bridge. L_{line} is supposed to be very small in practical system. i_{dc} is the product of three switching functions and three corresponding output currents. The peak value of i_{dc} is equal to that of the load current. Thus V_{PN} varies little in low frequencies. It is known that in SVM modulation, the summation of the three switch functions, S_{au}, S_{bu} and S_{cu}, varies from 0 to 3. Thus, V_{CM} varies from 0 V to V_{dc}, which is far large than the variation of V_{PN}. Thus, the CM noise source is much larger than DM noise source in low frequencies. Fig. 16 shows the CM noise source V_{CM} and the DM noise source V_{DM} got from simulation. It can be found that V_{CM} dominate the noise source in low frequency range while both are comparable in high frequency range. The reason is that the low frequency range of the noise source is dominated by the modulation method while the high
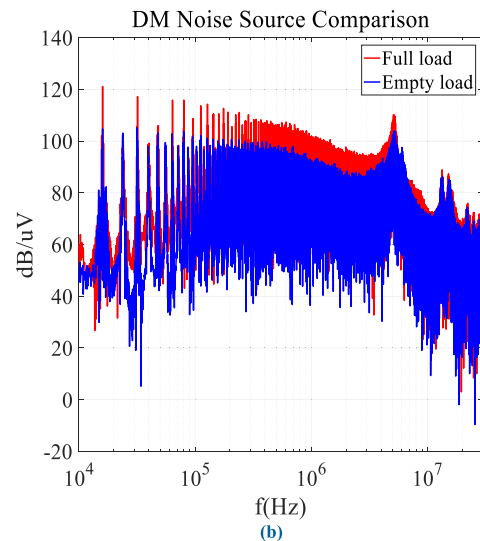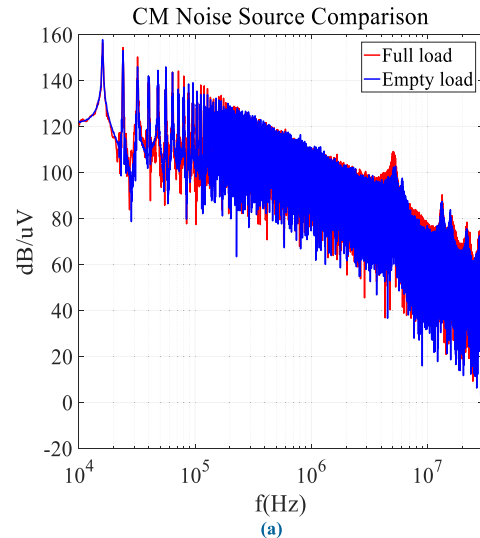
frequency part is caused by the device switching behavior and the resonance of the parasitic parameters.

As analyzed in Section III, there exists a remarkable difference in load characteristic between the CM and DM noise sources. The simulation results of the CM and DM noise sources got from (2), (3) and (4) for no load and full load are compared in Fig. 17. It can be found that the CM noise source varies little with the load situation in low frequency range while the DM noise source varies significantly. The DM noise is in significant higher level with full load than that with no load. From the results, it can be concluded that DM noise is load dependent while CM noise is load independent.

The predicted result of the total EMI noise got from simulation and the result got from experiment are compared in Fig. 18. The comparison is made in 10 kHz to 30 MHz range. The measurement is done using the voltage sampled on LISNs by an oscilloscope, and then calculated by FFT
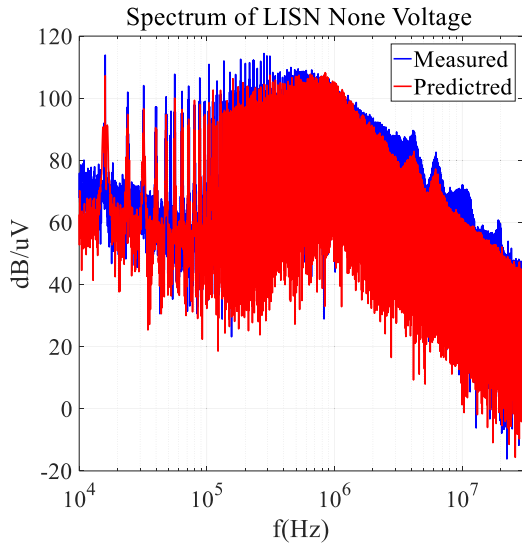
FIGURE 18. Comparison of the results from simulation and experiment.

FIGURE 19. Simulation result of the DM noise in normal case.

FIGURE 20. Simulation result of the CM noise in normal case.

to get the experiment result. It should be noted that an adequately large sampling frequency is needed for the accuracy of FFT calculation. The sampling frequency is chosen to be 250 MHz for both simulation and experiment in this study. Fig. 18 shows that the prediction result of the total EMI noise matches well with the measured result up to 30 MHz. A significant difference is found around 10 MHz, which is caused by the oscillation of the parasitic parameters of the inverter system. But in total, the error is within 10 dB up to 30 MHz.

From the above simulation and experiment results, we can conclude that the proposed model can predict the conducted emissions up to 30 MHz accurately. Moreover, DM noise is load dependent while CM noise is load independent. Thus, load situation can be used as the indicator for the MM noise observation.

B. SIMULATION AND EXPERIMENT RESULTS OF THE MIXED-MODE NOISE

The simulation results of the DM and CM noise are got by calculation with the help of Matlab. The DM and CM noise are defined as the algebraic operation of the voltage signals on LISNs, which can be got from (9). It should be noted that the 1 μF capacitors added to terminal *P* and terminal *N* are non- inductance polypropylene capacitors in the experiment. While in simulation, an ideal 1 μF capacitor model is added. The differences between the ideal capacitor and the practical polypropylene capacitor can cause differences between the simulation and the experiment results. However, the difference does not affect the analysis result of the mixed-mode noise.

The simulation results of the DM and CM noise in normal case, which means without any additional capacitors, are shown in Fig. 19 and Fig. 20 respectively. The red curves represent the total noise. The blue curves represent the noise
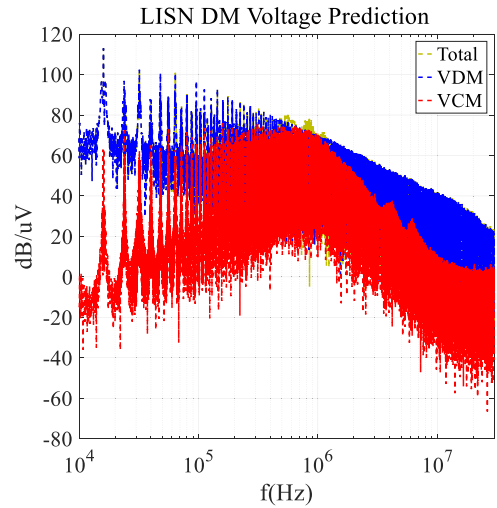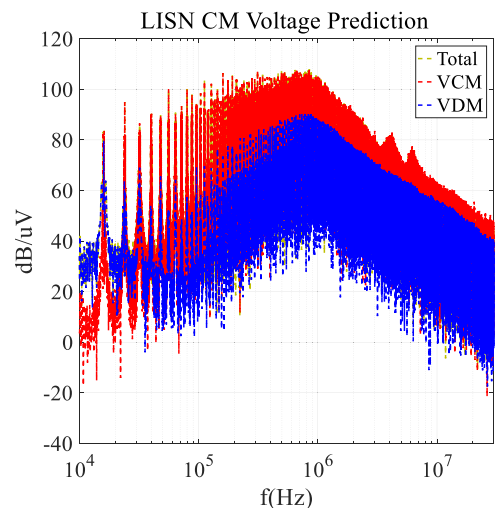
caused by the DM noise source. The orange curves represent the noise caused by the CM noise source. It can be concluded that the DM noise source determine the DM noise and the CM noise source determine the CM noise in normal case. The MM noise in the CM noise can also be ignored. This can be explained by (19). The weighting factors of the DM noise source and CM noise source are compared to each other in normal case, while the CM noise dominate the total noise source in the whole frequency range as shown in Fig. 20. Thus, the CM noise source dominates the CM noise and the MM noise can be ignored.

Fig. 21 and Fig. 22 show the simulation results of the CM noise with a 1 μF capacitor added to terminal P and terminal N respectively. The CM noise is main determined by the DM noise source in these two cases. From the analysis above, the weighting factor of the DM noise source is far larger than that of the CM noise source in these two cases, thus making DM noise source the major determinant. The MM
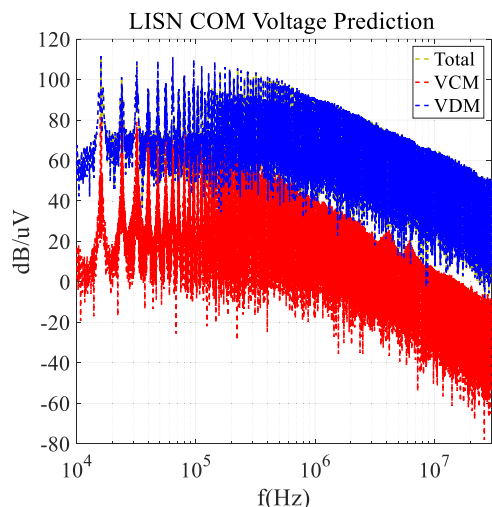
FIGURE 21. Simulation result of the CM noise with a 1 μF capacitor added to terminal P.
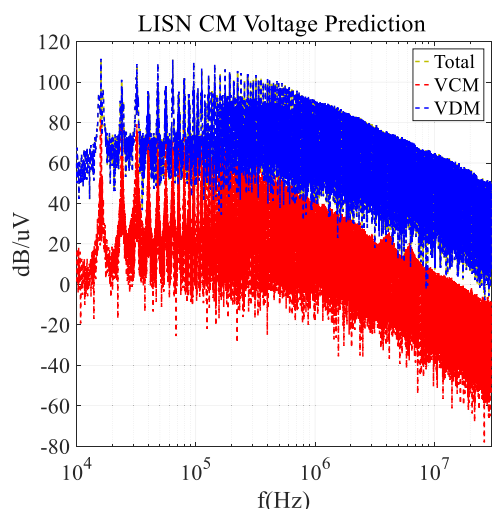

FIGURE 22. Simulation result of the CM noise with a 1 μF capacitor added to terminal N.

FIGURE 23. Experiment results of the CM noise with no load and full load in normal case.
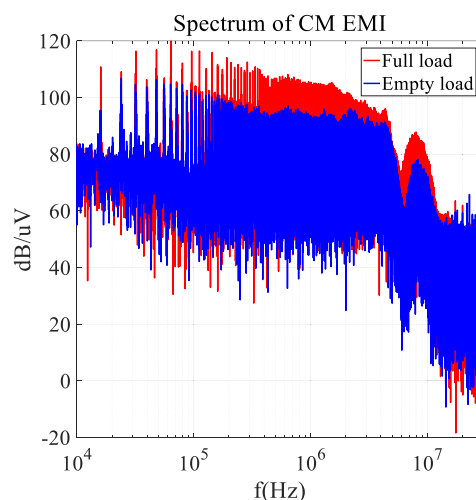
FIGURE 24. Experiment results of the CM noise with no load and full load when a 1 μF capacitor added to terminal P.
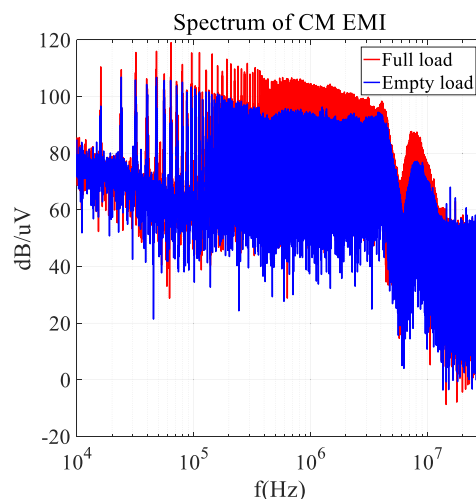
FIGURE 25. Experiment results of the CM noise with no load and full load when a 1 μF capacitor added to terminal N.

noise becomes obvious and dominates the CM noise in these two cases.

In real situation, it's very difficult to get the MM noise directly. Thus load current is used for the MM noise observation. Here no load and full load are taken as two extreme situations in the experiment. A remarkable difference can be observed on the DM noise source in these two situations. The experiment results of the CM noise with no load and full load in normal case are shown in Fig. 23. It shows that the CM noise changes little with load current in normal case, which means the CM noise source dominate the CM noise. Fig. 24 and Fig. 25 show the experiment results of CM noise with no load and full load when a 1 μF capacitor is added to terminal P and terminal N respectively. The CM noise changes obvious with load current in these two cases, which means the MM noise dominates the CM noise.
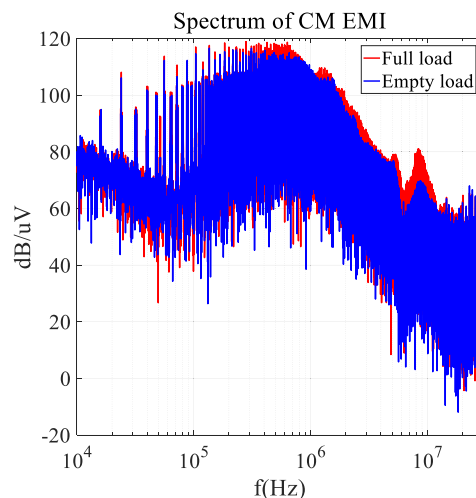
The above simulation and experiment results show that the three stray capacitors of the IGBT module dominate the

MM noise. If a significant difference is made between the capacitances of terminal P and N, the mixed-mode noise will become obvious and dominates the CM noise. The experiment results show good agreement with the simulation results, they both verify the analysis in Section III.

V. CONCLUSION

This paper proposed a novel frequency-domain EMC modeling technique for the conducted EMI prediction in a three-phase inverter system. The proposed model can predict the conducted emissions up to 30 MHz accurately. Then a three-terminal behavior model for analyzing MM noise is derived. It is shown that three stray capacitors of the IGBT module dominate the MM noise and the influence of the load current on the traditional CM and DM noise sources can be used for the MM noise observation. The accuracy of the posed model and the analysis of the MM noise are validated by the simulation and experiment results. The modeling technique and the method for analyzing MM noise can be extended to any other topology.

REFERENCES

[1] H. Akagi and T. Shimizu, "Attenuation of conducted EMI emissions from an inverter-driven motor," *IEEE Trans. Power Electron.*, vol. 23, no. 1, pp. 282–290, Jan. 2008.

[2] C. Jettanasen, F. Costa, C. Vollaire, B. Revol, and F. Morel, "Measurements and simulation of common mode conducted noise emissions in adjustable-speed AC drive systems," in *Proc. 20th Int. Zurich Symp. Electromagn. Compat.*, Jan. 2009, pp. 181–184.

[3] H. Akagi and T. Doumoto, "A passive EMI filter for preventing high-frequency leakage current from flowing through the grounded inverter heat sink of an adjustable-speed motor drive system," *IEEE Trans. Ind. Appl.*, vol. 41, no. 5, pp. 1215–1223, Sep. 2005.

[4] D. Boroyevich, X. Zhang, H. Bishinoi, R. Burgos, P. Mattavelli, and F. Wang, "Conducted EMI and systems integration," in *Proc. CIPS-8th Int. Conf. Integr. Power Electron. Syst.*, Nuremberg, Germany, Feb. 2014, pp. 1–14.

[5] M. Chaluvadi, G. Vincentraj, and K. G. Thomas, "A comparison study on conducted emission test in international EMC standards," in *Proc. IEEE Int. Conf. Power, Control, Signals Instrum. Eng. (ICPCSI)*, Sep. 2017, pp. 1352–1355.

[6] P. Hansen, "EMC standards update for Australia," in *Proc. Electromagn. Compat. Symp.-Melbourne*, Melbourne, VIC, Australia, Sep. 2010, pp. 1–5.

[7] *Industrial, Scientific and Medical Equipment-Radio-Frequency Disturbance Characteristics - Limits and Methods of Measurement*, Standard CISPR 11, 2019.

[8] *Electromagnetic Compatibility of Multimedia Equipment-Emission Requirements*, Standard CISPR 32, 2019.

[9] *Adjustable Speed Electrical Power Drive Systems—Part 3: EMC Requirements and Specific test Methods*, Standard IEC 61800-3, 2017.

[10] T. Misukka, L. Popova, "Improvement of IGBT model characterization with experimental tests," in *Proc. 15th Conf. EPE*, Sep. 2013, pp. 1808–1813.

[11] Y. Koyama, M. Tanaka, and H. Akagi, "Modeling and analysis for simulation of common-mode noises produced by an inverter-driven air conditioner," *IEEE Trans. Ind. Appl.*, vol. 47, no. 5, pp. 2166–2174, Sep. 2011.

[12] J. Meng, W. Ma, Q. Pan, L. Zhang, and Z. Zhao, "Multiple slope switching waveform approximation to improve conducted EMI spectral analysis of power converters," *IEEE Trans. Electromagn. Compat.*, vol. 48, no. 4, pp. 742–751, Nov. 2006.

[13] B. Revol, J. Roudet, J.-L. Schanen, and P. Loizelet, "EMI study of three-phase inverter-fed motor drives," *IEEE Trans. Ind. Appl.*, vol. 47, no. 1, pp. 223–231, Jan. 2011.

[14] B. Toure, J. Schanen, L. Gerbaud, T. Meynard, and J. Carayon, "EMC modeling of drives for aircraft applications: Modeling process, EMI filter optimization and technological choice," in *Proc. IEEE Energy Convers. Congr. Expo.*, Sep. 2011, pp. 1909–1916.

[15] X. Zhang, D. Boroyevich, P. Mattavelli, and F. Wang, "Filter design oriented EMI prediction model for DC-fed motor drive system using double Fourier integral transformation method," in *Proc. 7th Int. Power Electron. Motion Control Conf.*, vol. 2, Jun. 2012, pp. 1060–1064.

[16] H. Rebholz and S. Tenbohlen, "Prospects and limits of common- and differential-mode separation for the filter development process," in *Proc. Int. Symp. Electromagn. Compat. (EMC Eur.)*, Sep. 2008, pp. 1–6.

[17] H. Bishnoi, P. Mattavelli, R. Burgos, and D. Boroyevich, "EMI behavioral models of DC-fed three-phase motor drive systems," *IEEE Trans. Power Electron.*, vol. 29, no. 9, pp. 4633–4645, Sep. 2014.

[18] H. Bishnoi, A. C. Baisden, P. Mattavelli, and D. Boroyevich, "Analysis of EMI terminal modeling of switched power converters," *IEEE Trans. Power Electron.*, vol. 27, no. 9, pp. 3924–3933, Sep. 2012.

[19] A. C. Baisden, D. Boroyevich, and F. Wang, "Generalized terminal modeling of electromagnetic interference," *IEEE Trans. Ind. Appl.*, vol. 46, no. 5, pp. 2068–2079, Sep./Oct. 2010.

[20] H. Bishnoi, P. Mattavelli, R. P. Burgos, and D. Boroyevich, "EMI filter design of DC-fed motor-drives using behavioral EMI models," in *Proc. 17th Eur. Conf. Power Electron. Appl. (EPE ECCE-Europe)*, Sep. 2015, pp. 1–10.

[21] S. Qu and D. Chen, "Mixed-mode EMI noise and its implications to filter design in offline switching power supplies," *IEEE Trans. Power Electron.*, vol. 17, no. 4, pp. 502–507, Jul. 2002.

[22] H.-I. Hsieh, D. Chen, and S. Qu, "A filter design procedure incorporating mixed-mode EMI noise for off-line switching power supplies," in *Proc. 4th IPEMC*, vol. 3, Aug. 2004, pp. 1527–1532.

[23] H.-I. Hsieh, "Effects of mix-mode noise emissions on the design method of power factor correction boost rectifier EMI filters," in *Proc. Int. Power Electron. Conf. (ECCE ASIA)*, Jun. 2010, pp. 2438–2443.

[24] M. M. Jha, K. B. Naik, and S. P. Das, "Types of electro magnetic interferences in SMPS and using Y-capacitor for mitigation of mixed mode noise," in *Proc. Int. Conf. Power, Control Embedded Syst.*, Nov. 2010, pp. 1–6.

[25] M. Jin and M. Weiming, "A new technique for modeling and analysis of mixed-mode conducted EMI noise," *IEEE Trans. Power Electron.*, vol. 19, no. 6, pp. 1679–1687, Nov. 2004.

[26] J. Xue and F. Wang, "Mixed-mode EMI noise in three-phase DC-fed PWM motor drive system," in *Proc. IEEE Energy Convers. Congr. Expo.*, Sep. 2013, pp. 4312–4317.

[27] B. Sun, R. Burgos, X. Zhang, and D. Boroyevich, "Differential-mode EMI emission prediction of SiC-based power converters using a mixed-mode unterminated behavioral model," in *Proc. IEEE Energy Convers. Congr. Expo. (ECCE)*, Sep. 2015, pp. 4367–4374.

[28] W. Zhou, X. Pei, Y. Kang, and Y. Xiang, "A new technique for modeling and analysis of electromagnetic interference in three-phase inverter system," in *Proc. IECON-43rd Annu. Conf. IEEE Ind. Electron. Soc.*, Oct./Nov 2017, pp. 6983–69880.

[29] Y. Xiang, X. Pei, W. Zhou, Y. Kang, and H. Wang, "A fast and precise method for modeling EMI source in two-level three-phase converter," *IEEE Trans. Power Electron.*, vol. 34, no. 11, pp. 10650–10664, Nov. 2019.

[30] M. Hosoya, "The simplest equivalent circuit of a multi-terminal network," *Bull. College Sci. Univ. Ryukus*, vol. 70, pp. 1–10, Sep. 2000.

WU ZHOU received the B.S. degree in electrical engineering from the Huazhong University of Science and Technology (HUST), Wuhan, China, in 2012, where he is currently pursuing the Ph.D. degree in electrical engineering. His major research interests include high-power drive systems and EMI.

XUEJUN PEI (Senior Member, IEEE) received the B.E., M.E., and Ph.D. degrees in electrical engineering from the Huazhong University of Science and Technology, Wuhan, China, in 1998, 2001, and 2004, respectively.

In 2004, he joined the Huazhong University of Science and Technology, as a Teaching Assistant. Since 2006, he has been a Full Professor with the College of Electrical and Electronic Engineering. His research interests focus on high-power converter, EMC issue, fault diagnosis of power electronics, and the related application in the power systems.

YANGXIAO XIANG received the B.S. degree in electrical engineering and automation from Sichuan University, Chengdu, China, in 2014. He is currently pursuing the Ph.D. degree in electrical engineering from the Huazhong University of Science and Technology, Wuhan, China. His major research interests include electromagnetic compatibility of the power conversion.

YONG KANG was born in Hubei, China, in 1965. He received the B.E., M.E., and Ph.D. degrees from the Huazhong University of Science and Technology (HUST), Wuhan, China, in 1988, 1991, and 1994, respectively.

In 1994, he joined the School of Electrical and Electronic Engineering, HUST, where he became a Professor, in 1998. He is the author or coauthor of more than 200 technical articles published in journals and conferences. His research interests include power electronic converter, ac drives, electromagnetic compatibility, and renewable energy generation systems.

Dr. Kang received the Delta Scholar Award from the Delta Environmental and Educational Foundation, in 2005, and supported by the Program for New Century Excellent Talents in University from the Chinese Ministry of Education, in 2004. He is currently serving as the Vice Chairman of the China UPS standard committee and an Associate Editor for the *Journal of Power Electronics*.

●●●